

Autonomous Navigation around Phobos: Applications to the Martian Moons eXploration mission.

Edoardo Ciccarelli¹ Nicola Baresi²

¹PhD candidate, University of Surrey, Guildford, UK
Email: e.ciccarelli@surrey.ac.uk

²Lecturer, University of Surrey, Guildford, UK
Email: n.baresi@surrey.ac.uk

Abstract—Proximity operations around Phobos are critical for the Martian Moons eXploration (MMX) mission, and accurate knowledge of the spacecraft’s trajectory is required to perform scientific observations and maximise the chances of understanding the moon’s internal structure. Possible solutions to implement autonomous navigation around Phobos while orbiting at lower altitudes are presented in this paper and compared with standard navigation techniques. For this purpose, our analyses will compare the level of knowledge achievable once the connection with the Deep Space Network is cut off, showing what can be achieved without ground support, using only information that can be collected and processed onboard, mainly lidar and optical data. Different strategies to build a map of the moon’s surface’s landmarks are also discussed, demonstrating how this operation can be performed autonomously by the spacecraft and how landmark-based navigation is paramount in estimating the spacecraft’s state. Finally, the capability of this setup to observe the moon’s gravity field will be assessed, returning precious information for the future geodetic investigations of the Martian Moons eXploration mission around Phobos.

I. INTRODUCTION

The origin of the two Martian moons, Phobos and Deimos, remains unknown to the astronomical community. One of the most accredited theories is that they may be asteroids captured by Mars’s gravity field, as suggested by their small and irregular shape, and could therefore provide a unique insight into the history of the early solar system material’s migration towards the inner planets. Nevertheless, their surprisingly circular and equatorial orbits clash with this hypothesis, suggesting that they may have formed in situ, following a giant impact on Mars, similar to what happened to the Earth-Moon system, or during the planet’s accretion period [1].

The Martian Moons eXploration (MMX) mission, planned for launch in 2026, aims to shed light on the origin of the two moons by performing a prolonged observation of Phobos. The spacecraft will be placed on periodic and quasi-periodic quasi-satellite orbits (QSOs), with different geometries around the moon, moving between different heights from the surface and collecting samples. It will also perform several flybys of Deimos before finally returning to Earth with the collected samples. During this proximity phase around Phobos, accurate knowledge of the spacecraft’s trajectory is required to perform scientific observations and reconstruct the moon’s internal structure. Strong perturbations govern the spacecraft’s

dynamics at low altitudes owing to the strong influence of the nearby Mars and the moon’s irregular shape, but while this can be a challenge for the spacecraft’s flight, it can also be exploited to extract precious information about the moon’s internal structure.

We present in this paper solutions to navigate around Phobos during the MMX proximity phase, either autonomously or with ground support. Our analysis exploits lidar and optical data to navigate the spacecraft, extracting and exploiting the limb of the red planet, features on the moon’s surface, and line of sight direction vectors towards Deimos when in the field of view. With this aim, we will also suggest strategies to autonomously identify points of interest on the moon’s surface that could then be used for landmarks-based relative navigation. For this purpose, synthetic images have been generated in Blender using the Orochi camera’s specifications, to simulate the in-orbit spacecraft’s point of view and quantify the amount of landmarks that can be mapped from the pictures. The effects of cutting off the connection with the Deep Space Network (DSN) will be investigated, highlighting how the navigation performances deteriorate without ground support. The extracted observables at the epoch are then processed with a Kalman filter to estimate the spacecraft’s and Phobos’s state vectors’ uncertainties and the moon’s spherical harmonics coefficients. The results of this covariance analysis will support the geodetic investigations of the Martian Moons eXploration mission around Phobos.

II. DYNAMICAL MODEL

The dynamics that describe the system’s motion are defined in the Phobos-fixed reference frame, whose axes are aligned with the moon’s principal axes of inertia and the origin in its centre of mass, as represented in Fig. 1 [2].

In this system, Mars appears to move in the sky oscillating back and forth along the radial direction, and Phobos’ libration motion is reflected as a motion of Mars around the system’s x axis. High interest is given to the libration motion of Phobos in this analysis since, as reported in [2], its amplitude is a function of the moon’s moments of inertia and the mass ratio between the two bodies, and it could therefore be used to gather information about the moon’s internal structure. This libration amplitude can be observed by tracking the

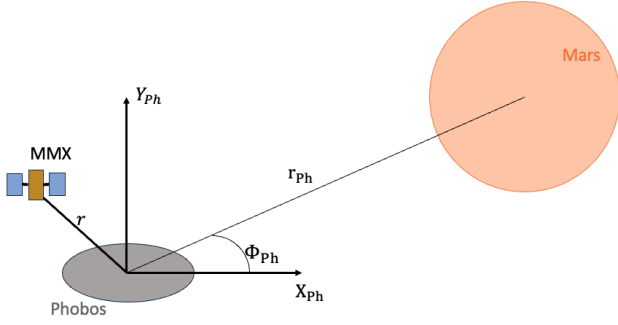


Fig. 1: Schematic representation of the problem's geometry.

spacecraft's motion, around the moon, for which a harmonic expansion of Phobos's gravitational field is also considered, and the effect of Mars' oblateness is taken into account.

The complete state vector of the system for the analysis is therefore composed of the spacecraft's position and velocity $\mathbf{X}_{MMX} = [\mathbf{r}, \mathbf{v}]$, the states describing Mars's apparent motion in the sky \mathbf{X}_M , the harmonics coefficients of the moon's gravitational field ($C_{0,0}$, $C_{1,0}$, $C_{1,1}$, etc.), and some biases affecting the spacecraft's sensors (ϵ_ρ , $\epsilon_{v_{camera}}$, etc.). The state vector is then defined as:

$$\mathbf{X} = [\mathbf{X}_{MMX}, \mathbf{X}_M, C_{0,0}, \dots, \epsilon_{v_{camera}}] \quad (1)$$

The dynamics of the system can be described by a system of first-order differential equations of this state vector. The different dynamics within this system are described in the following sections, starting from the characterization of how Phobos' motion around Mars can be reflected in the apparent motion of the red planet in the sky.

A. Phobos's motion

The potential describing the roto-translational coupling of an oblate primary body and a smaller ellipsoidal secondary body was derived in [2]. In the case of the Mars-Phobos system, adopting the subscripts "M" and "Ph" to indicate respectively Mars's and Phobos's quantities, this potential can be written as:

$$\begin{aligned} V(r_{Ph}, \Phi_M, \Phi_{Ph}) = & -\frac{GM_M M_{Ph}}{r_{Ph}} \left\{ 1 + \frac{1}{2r_{Ph}^2} \left[Tr(\bar{\mathbf{I}}_1) + \right. \right. \\ & + Tr(\bar{\mathbf{I}}_2) - \frac{3}{2}(I_{1x} + I_{1y} - \cos(2\Phi_M)(I_{1y} - I_{1x}) + \\ & \left. \left. + I_{2x} + I_{2y} - \cos(2\Phi_{Ph})(I_{2y} - I_{2x})) \right] \right\} \end{aligned} \quad (2)$$

with Φ_M and Φ_{Ph} being Mars's and Phobos's libration angles respectively, $\bar{\mathbf{I}}_1$ and $\bar{\mathbf{I}}_2$ the inertia tensors of the two bodies, $Tr(\cdot)$ the trace operator of a matrix, and I_{1x} , I_{1y} , I_{2x} , and I_{2y} being the inertia tensor's components.

The authors in [2], out of some considerations on the system's integrals of motion and the small entity of the main

body's libration amplitude, derived the equations of motion in the rotating frame centred on the smaller body, as:

$$\begin{aligned} \ddot{r}_{Ph} &= \frac{(K - \bar{I}_{2z} \dot{\Phi}_{Ph}) r_{Ph}}{I_z^2} - \frac{1}{\nu} \frac{\partial V}{\partial r_{Ph}} \\ \ddot{\Phi}_{Ph} &= - \left(1 + \frac{\nu r_{Ph}^2}{\bar{I}_{2z}} \right) \frac{1}{\nu r_{Ph}^2} \frac{\partial V}{\partial \Phi_{Ph}} + \frac{2\dot{r}_{Ph}(K - \bar{I}_{2z} \dot{\Phi}_{Ph})}{r_{Ph} I_z} \end{aligned} \quad (3)$$

with K being the free angular momentum of the system and ν the mass ratio between the two bodies. Their definition and the partial derivatives of the potential required by these equations of motion are described in [2] and here recalled:

$$\begin{aligned} \nu &= \frac{M_M}{M_M + M_{Ph}} \\ K &= K_{tot} - K_1 = I_z \dot{\theta} + \bar{I}_{Phz} \dot{\Phi}_{Ph} \\ \frac{\partial V}{\partial r_{Ph}} &= \frac{\nu}{r_{Ph}} \left\{ 1 + \frac{3}{2r_{Ph}^2} \left[(\bar{I}_{1z} - \bar{I}_s) - \frac{1}{2} \bar{I}_{2x} - \frac{1}{2} \bar{I}_{2y} + \right. \right. \\ & \left. \left. + \bar{I}_{2z} + \frac{3}{2} (\bar{I}_{2y} - \bar{I}_{2x}) \cos(2\Phi_{Ph}) \right] \right\} \\ \frac{\partial V}{\partial \Phi_{Ph}} &= \frac{3}{2} \frac{\nu}{r_{Ph}^3} (\bar{I}_{2y} - \bar{I}_{2x}) \sin(2\Phi_{Ph}) \end{aligned} \quad (4)$$

θ is the Phobos's true anomaly in the moon's perifocal reference frame which can be included in the state vector, propagated and observed as a state of the system due to its direct relation with the moon's free angular momentum and libration rate.

$$\dot{\theta} = \frac{K - \bar{I}_{2z} \dot{\Phi}_{Ph}}{I_z} \quad (5)$$

B. MMX motion

For what concerns the probe's dynamics, only gravitational accelerations are considered acting on MMX, therefore its motion can be described in the rotating frame centred on Phobos as described in [3]:

$$\begin{aligned} \dot{\mathbf{r}} &= \mathbf{v} \\ \dot{\mathbf{v}} &= \mathbf{g}_{Ph} + \mathbf{g}_M - \dot{\boldsymbol{\Omega}} \times \mathbf{r} - 2(\boldsymbol{\Omega} \times \mathbf{v}) - \boldsymbol{\Omega} \times (\boldsymbol{\Omega} \times \mathbf{r}) \end{aligned} \quad (6)$$

with \mathbf{g}_{Ph} and \mathbf{g}_M being the gravitational accelerations due to Phobos and Mars, respectively, and $\boldsymbol{\Omega}$ being the angular velocity of the system causing the Euler, Coriolis and centrifugal accelerations.

The acceleration due to Phobos is modelled as a fourth-degree and order spherical harmonics expansion of the moon's gravitational potential, as reported in [4]:

$$\begin{aligned} U(x, y, z) = & \frac{\mu_{Ph}}{r} \left[1 + \sum_{n=2}^{\infty} \sum_{m=0}^n \left(\frac{R}{r} \right)^n P_{n,m}(\sin \phi_{gc}) \right. \\ & \left. (C_{n,m} \cos(m\lambda) + S_{n,m} \sin(m\lambda)) \right], \end{aligned} \quad (7)$$

where $P_{n,m}$ are the associated Legendre polynomials, ϕ_{gc} is the latitude of the satellite, λ is the longitude of the satellite, and $C_{n,m}$ and $S_{n,m}$ are the n-degree and m-order Stokes' coefficients. Finally, $R = 11.107$ km is the Phobos's reference

sphere radius and the distance of the spacecraft from its centre is simply r .

For what concerns the acceleration caused by Mars, the red planet is instead modelled as an oblate spheroid [5]:

$$\mathbf{g}_M = -\frac{\mu_M}{r_M^3} \left(1 + J_2 \left(\frac{R_M}{r_M} \right)^2 \begin{bmatrix} 1 - 3 \left(\frac{z}{r_M} \right)^2 \\ 1 - 3 \left(\frac{z}{r_M} \right)^2 \\ 3 - 5 \left(\frac{z}{r_M} \right)^2 \end{bmatrix} \right) \mathbf{r}_M - \frac{\mu_M \mathbf{r}}{r^3} \quad (8)$$

where in this case μ_M is the gravitational parameter of Mars, R_M is the planet's equatorial radius, J_2 is the second zonal harmonic of the planet's gravitational field and \mathbf{r}_M is the position vector of the spacecraft with respect to Mars.

For what concerns the reference frame's angular velocity, we have to consider that while the moon librates, it also rotates around Mars, therefore the angular velocity of the system can be written as:

$$\boldsymbol{\Omega} = [0, 0, \dot{\theta} + \dot{\Phi}_{Ph}] \quad (9)$$

$\boldsymbol{\Omega}$ is not constant and its time derivative $\dot{\boldsymbol{\Omega}}$ is consecutively not null, causing the spacecraft to experience the whole set of Euler, Coriolis and centrifugal accelerations.

C. Reference trajectories definition

QSOs, 3DQSOs and SwingQSOs, designed in the years as reference science trajectories for MMX, were initially designed in the Hill problem's dynamics by Baresi *et al.* [6]. As in [7], an optimization procedure was performed to find the best initial conditions that in this new dynamical model would allow the spacecraft to move along the same orbits. Once these initial conditions were found, the spacecraft's motion was propagated in the Mars-Phobos system's dynamics, and the results were saved as SPICE's .bsp files to be used as ground truth trajectory for the covariance analysis. Observables data were simulated along these trajectories, using the models described in the following sections, to be then processed by a UKF-based covariance analysis tool, equivalent to the one described in [7], that quantifies the state vector components and the moon's spherical harmonics coefficients' uncertainties.

III. OBSERVABLES

Six data types were considered for this numerical analysis and are processed to navigate: radiometric data from Earth-based ground stations, lidar measurements spanning the moon's surface, surface's landmarks position in the collected pictures, the Mars's limb apparent dimension and the line of sight direction vector towards Deimos. The mathematical model and acquisition frequency for each are described in the following paragraphs.

A. DSN-based observables: Range & Range Rate

The covariance analyses carried out in this study used an idealized range and range-rate measurement between MMX and Earth, thereby delegating clock errors, atmospheric effects,

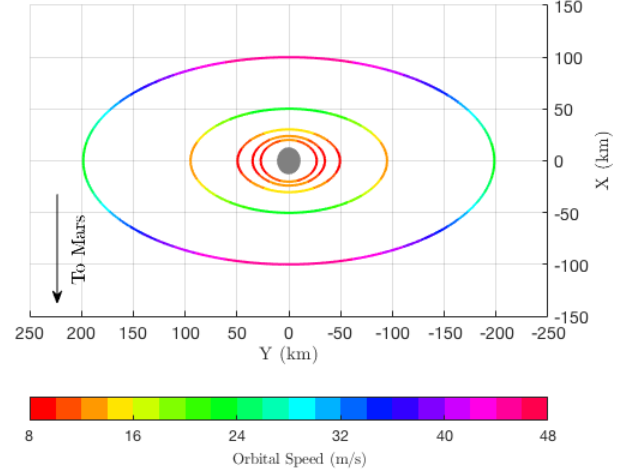


Fig. 2: The five altitude MMX candidate QSO orbits around Phobos [6].

and time delays to the bias ϵ_ρ [8]. Following these assumptions, the range measurements are defined as

$$\rho = G(\mathbf{X}) + \epsilon = \sqrt{(\mathbf{r}_E - \mathbf{r}_{St_i})^T (\mathbf{r}_E - \mathbf{r}_{St_i})} + \epsilon_\rho \quad (10)$$

where \mathbf{r}_E and \mathbf{r}_{St_i} are the MMX's and i^{th} ground station's position vectors as seen from the Earth-centered J2000 inertial frame, respectively, and ϵ_ρ is a bias affecting this range measurements, which is also part of the state vector.

Similarly,

$$\dot{\rho} = \frac{(\mathbf{r}_E - \mathbf{r}_{St_i})^T (\dot{\mathbf{r}}_E - \dot{\mathbf{r}}_{St_i})}{\rho} + \epsilon_{\dot{\rho}} \quad (11)$$

where $\dot{\mathbf{r}}_E$ and $\dot{\mathbf{r}}_{St_i}$ are the velocity vectors of the spacecraft and ground station, respectively, and $\epsilon_{\dot{\rho}}$ is the bias affecting the range rate data.

Note that occultation checks were performed throughout these numerical simulations, thereby preventing measurements from being collected whenever MMX was below the stations' local horizons or eclipsed by Mars or Phobos. The DSN antennas in Madrid, Canberra, and Goldstone have been considered, and measurements are collected at intervals of once per hour for the range and once per ten minutes for the range rate [9].

B. Lidar

A lidar device typically emits an electromagnetic signal and listens for the echo of the same signal once it bounces off the surface of a celestial body. As an electromagnetic signal, it travels at the speed of light; therefore, measuring the time distance between the emission and the reception of the echo provides information on the relative distance between Phobos and MMX. Considering the ellipsoidal shape of Phobos as a first-order approximation yields a state-observation relationship of the form [10]:

$$\rho_{Lidar} = \sqrt{\mathbf{r}^T \mathbf{r}} - R_{Ph}(\lambda, \phi) + \epsilon_{Lidar} \quad (12)$$

where R_{Ph} is the radius of the ellipsoidal Phobos as a function of the spacecraft's latitude (λ) and longitude (ϕ), defined in the moon-fixed reference frame, and ϵ_{Lidar} is a bias affecting the lidar. As per [11], MMX's lidar has an acquisition frequency ranging between 1 and 4 Hz. An analysis was performed regarding the effects of this frequency on estimation performance, and it was found that the envelopes have a plateau for frequencies higher than one measurement every 2 minutes, identifying this value as the lidar acquisition frequency for the analysis. Furthermore, MMX's onboard lidar has an operational range of 100 m-100 km; therefore, no measurements outside this range are collected.

C. Features

To be able to perform landmark-based navigation, the spacecraft needs a map of the moon's surface to be able to recognise different points of interest, and then match them with the features extracted from the pictures that it collects while in orbit and orient itself against them. This poses the need for a surface mapping strategy, to be implemented at different altitudes from the moon's surface, to be able to collect an iteratively more detailed map of the moon's surface.

1) *Phobos's surface mapping strategy*: This process must be performed considering the spacecraft's orbit around the moon that will observe illumination changes caused by both the moon's rotation around Mars and the spacecraft's motion around Phobos.

As reported by Baresi *et al.* [6], the revolution period of the spacecraft around Phobos is expected to range between 4 and 8 hours, depending on the specific orbit the spacecraft is in. This revolution period is, especially for the lower altitudes, shorter than the time it takes for the spacecraft to move from the day side to the night side of the moon (which spans from almost 14 days for the QSO-H to around 5 hours for the QSO-La, QSO-Lb and QSO-Lc orbits). This means that the spacecraft can observe the complete moon's surface and collect pictures of it which can be used to build such a map. Figure 3 shows the situation for the QSO-La orbit, whose revolution period is 5.76 hours, making of it the borderline case for completing the observation of the moon's surface in one orbit.

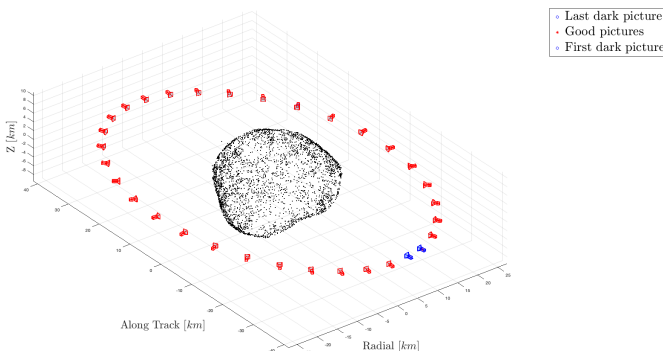


Fig. 3: Coverage of the moon's surface orbiting the QSO-La orbit while taking a picture every ten minutes.

Once such a database of pictures is available there are several strategies which could be performed, also autonomously



Fig. 4: Some examples of the synthetic pictures generated with Blender from the point of view of MMX during the QSO-La (bottom) orbits. The 3D models of Phobos were downloaded from NASA's repository, while Mars and its atmosphere were generated from scratch, as well as the Sun and its effects on the camera when in the field of view.

by the spacecraft, to build a map of points of interest. The spacecraft could collect pictures while on the Sun-lit side of the moon to process them with a Bundle Adjustment algorithm during the passage through the night side. These operations can be performed onboard if enough data storage and computational power are available, or on the ground if the spacecraft can transmit this picture database to Earth. Alternatively, Simultaneous Localization and Mapping (SLAM) algorithms are an iterative way to autonomously build a catalogue of landmarks, while estimating the spacecraft's position at the pictures' epoch. Synthetic images have been generated to simulate the in-orbit spacecraft's point of view and they have been fed to a monocular SLAM algorithm to quantify the amount of landmarks that can be mapped from the pictures. The resulting point cloud of the moon's surface's features was then used as a map to perform landmark-based navigation.

2) *Observable modelisation*: The principles of perspective projection can be used to describe the relationship between the position of surface features on the Phobos surface with their position in the camera's field of view and the spacecraft's position. The main hypothesis here is based on the availability of the previously described map of Phobos's surface's features, and that the features within are properly differentiable from each other. The optical properties of the OROCHI camera are reported in Table I [1], [12]: Therefore, assuming a pinhole

TABLE I: Optical properties of the OROCHI camera.

Parameter	Value
Focal length	15 mm
Sensor size	36 × 24 mm
Camera resolution	3296 × 2472 pixel

camera model, the camera's intrinsic matrix is:

$$\mathbf{K} = \begin{bmatrix} f_x & 0 & c_x \\ 0 & f_y & c_y \\ 0 & 0 & 1 \end{bmatrix} = \begin{bmatrix} 1373.3 & 0 & 1648 \\ 0 & 1545 & 1236 \\ 0 & 0 & 1 \end{bmatrix} \quad (13)$$

The camera extrinsic matrix can be reconstructed as:

$$\mathbf{M}_{ext} = \begin{bmatrix} \mathbf{R} & \mathbf{r} \\ \mathbf{0}_{(1 \times 3)} & 1 \end{bmatrix} \quad (14)$$

with \mathbf{R} being the rotation matrix from the moon-fixed to the camera reference frame and \mathbf{r} being the camera's position from

the moon's centre of mass, which we assume to be the same as the spacecraft's position vector. The projection matrix for the OROCHI camera is then defined as:

$$P = K[R|t] \quad (15)$$

where R and t are the rotation matrix and translation vector that describes the camera's position with respect to the moon-fixed reference frame. The projection of a feature in the camera's field of view is then defined as:

$$p = \begin{bmatrix} u + \epsilon_u \\ v + \epsilon_v \end{bmatrix} = P X_f + \begin{bmatrix} \epsilon_u \\ \epsilon_v \end{bmatrix} \quad (16)$$

where X_f is the position of the feature in the moon-fixed reference frame and ϵ_u and ϵ_v are the camera's biases in the sensor's x and y directions. In this analysis, the nadir-

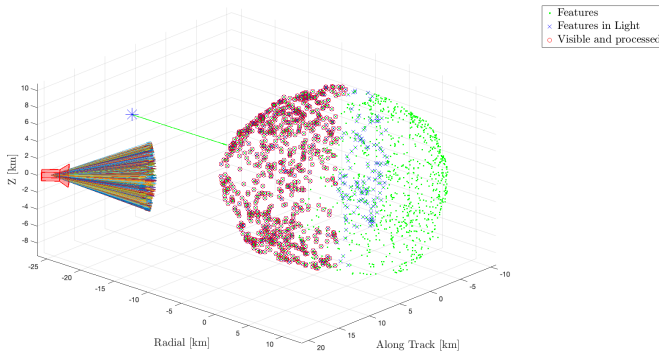


Fig. 5: Visualization of the features' identification and extraction processes within the camera's field of view.

pointing spacecraft's camera takes a picture every ten minutes, and the features are extracted from the pictures and matched with the map of the moon's surface whenever they are in light conditions and the camera can observe them.

D. Limb

Celestial bodies' limbs and their size in the field of view of a camera can be used to estimate the distance between the spacecraft and the body itself. This technique has been used in the past to navigate in the cislunar space, in the Martian, Jupiter's and Saturn's system, and several studies have been published on the topic [13]–[15]. The idea relies on the fact that the apparent size of different bodies, inside of a picture, is inversely proportional to the distance between the spacecraft and the body. Therefore, if the actual size of the body is known, this apparent size can be used to estimate the distance between the spacecraft and the body.

The relationship between the apparent size of the body in the picture and the distance between the spacecraft and the body was modelled as:

$$D = f \left(\frac{D_T}{r} \right) \quad (17)$$

where D is the target body's diameter, f is the focal length of the camera, D_T is the apparent size of the body in the picture, and r is the distance between the camera and the celestial body of interest.

Information about the Mars limb's apparent size is extracted from the same pictures used to perform the landmark-based navigation, which are taken every ten minutes. This observable is used only if the planet's disk is not hidden by Phobos's silhouette.

E. Observing Deimos

Similarly to Mars, Deimos can also be used to extract useful information about the spacecraft's state. Since it is orbiting Mars further away than Phobos, it should appear in the opposite direction of the red planet with respect to the spacecraft. Due to the moon's small size, the apparent motion of Deimos in the sky is expected to appear as a slowly drifting bright spot in the camera's field of view. However, when properly in opposition, it may occupy more than one pixel in the pictures. The same biases affecting the camera's sensor are considered, and knowledge of the true position of Deimos is considered to be available onboard the spacecraft. Its position, defined at any time in the Phobos-fixed reference frame, is rotated and translated in the camera reference frame and projected in the camera's sensor with the OROCHI's pinhole camera model (Eq.13) and perspective projection fundamentals described in the previous section (Eq.16).

A picture of Deimos is collected every ten minutes if the moon is expected to be in the field of view; not hidden by the silhouette of Phobos and only if Mars is not expected to appear in the same picture. This was decided as the red planet is expected to be much brighter than Deimos, and its presence in the same picture would make the moon's observation impossible.

IV. ANALYSIS SETUP

Observations between MMX and the DSN ground stations are generated together with Lidar measurements of the MMX-Phobos distance and synthetic pictures, while the spacecraft moves along the orbits. All of the measurements are corrupted with zero-mean Gaussian white noise, whose standard deviations are reported in Table II. The white noise values for the ground station data were obtained from [9], and the noise added to the lidar measurements was recovered from technical data on MMX's onboard instrumentation [11]. The pixel noise was instead assumed to be 0.2 pixel, as reported in [16]. A stochastic acceleration of $10^{-10} km/s^2$ was used as the process noise in the covariance analysis tool to account for unmodelled dynamics such as solar radiation pressure (SRP) and non-gravitational accelerations (NGA) affecting MMX's motion.

TABLE II: Standard deviation of the white noise added to the observations [17].

Measurement	Frequency	Noise standard deviation
Range	1 hour	$\sigma_\rho=2$ m
Range rate	10 min	$\sigma_{\dot{\rho}}=3 \times 10^{-4}$ m/s
Lidar range	2 min	$\sigma_{lidar}=10$ m
Pictures	10 min	$\sigma_{camera}=0.2$ pixel

The *a priori* uncertainties for the states at the beginning of the covariance analysis are listed in Table III. MMX's initial

uncertainties were assumed [17], to have $3\sigma \simeq 1$ km for the position vector components and $3\sigma \simeq 1$ m/s for the velocity vector components.

TABLE III: A priori uncertainties for the problem state vector components.

Object	Estimated parameter	σ a priori uncertainty
MMX	Position components	300 m
	Velocity components	0.3 m/s
Phobos	Radial distance	100 m
	Radial velocity	0.1 m/s
	Libration angle	0.3 rad
	Libration velocity	1×10^{-3} rad/s
	Harmonics coefficients	1×10^{-2}
Bias	Range	1 km
	Range rate	1 m/s
	Lidar	1 km
	u_{Camera}	1 pixel
	v_{Camera}	1 pixel

Data acquisition campaigns are simulated for each orbit, and the data are fed into the covariance analysis tool described in [7] to study the behaviour of the state vector components' 3σ covariance envelopes.

V. RESULTS

Our analysis was focused on two main objectives: the first was the assessment of the spacecraft's capability to autonomously navigate around Phobos without ground support. This could be certified by observing the behaviour of the state vector components' uncertainties once only spaceborne data are processed and comparing the results with the ones obtained when DSN data are used. The second objective was the assessment of the spacecraft's capability to observe the moon's gravity field and the quality of information that can be extracted from the data collected during the proximity phase around Phobos. The results of this covariance analysis are reported in the following sections, where these two objectives are addressed with different setups and lengths of data collection campaigns.

A. Relative navigation performance

Figure 6 shows the 3σ covariance envelopes for MMX's position and velocity vector components, and the RMS of the state vector components' uncertainties, for one day of data collected while orbiting the QSO-Lb orbit, the second lowest represented in Figure 2.

The first thing to note is the entity of the position vector uncertainties, which are in the order of a few meters, and of the velocity vector uncertainties, which span in the order of a few millimetres per second. The position uncertainties show a clear periodic behaviour, with time windows in which the spacecraft can take and process pictures of the moon's surface and its features, and others in which it is on the night side of the moon and the only available data are the radiometric and lidar measurements. The optical data's contribution to shrinking the state vector's uncertainties is evident, as the position uncertainties are at their minimum when the spacecraft is on the day side of the moon. The amount of landmarks that can

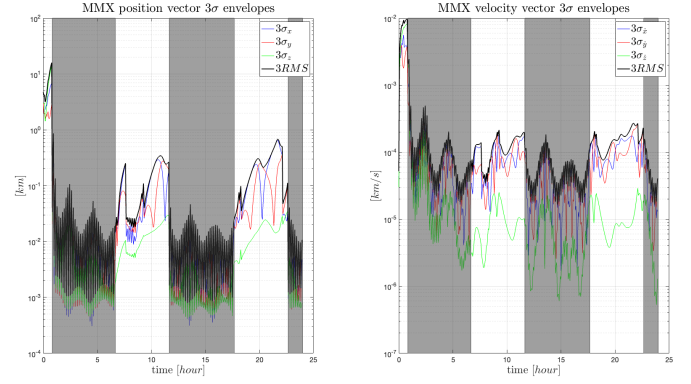


Fig. 6: MMX's 3σ state vector components' covariance envelopes, and RMS, for one day of data processing the full set of observables, radiometric data included. The shaded areas represent the intervals in which the spacecraft can take and process pictures of the moon's surface.

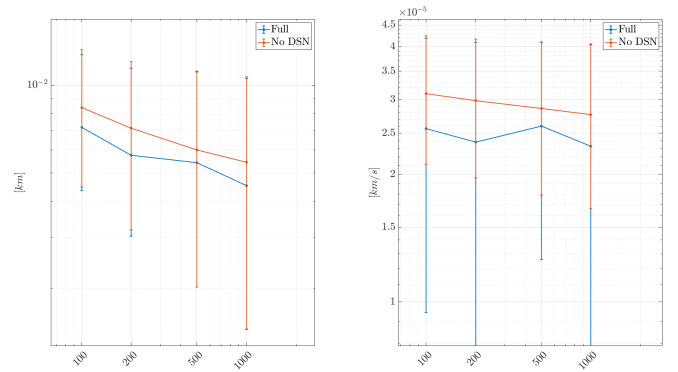


Fig. 7: Position and velocity vectors' components' RMS as a function of the number of features extracted from the pictures from the QSO-Lb orbit.

be extracted from the pictures is expected to be a key factor in the quality of the navigation performance.

For this analysis, the landmarks' database was assumed to be the same as the one extracted from the data collected in a revolution around Phobos processed by a monocular SLAM algorithm, one of the techniques suggested in the previous section to autonomously build the moon's surface map. Nevertheless, Figure 7 shows the decay of the state vector components' uncertainties' RMS as a function of the average number of the surface's recognised landmarks for the QSO-Lb orbit. The mean value of these uncertainties' RMS is reported here, in one of the orbit's branches in which the spacecraft can observe surface landmarks, with error bars representing the maximum and minimum oscillations of the envelopes around it. The RMS of the position vector components' uncertainties is seen to be inversely proportional to the number of features extracted from the pictures, and the relationship to be retained also when DSN radiometric data are not available.

For what concerns the remaining state vector components, the libration angle's uncertainty is seen to be in the order of a few millidegrees, and its rate's uncertainty is in the order

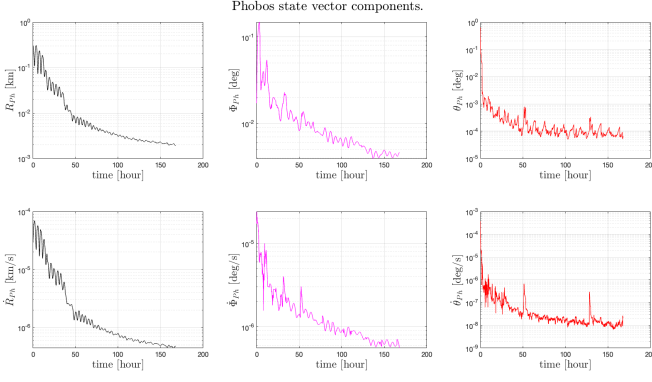


Fig. 8: Phobos's 3σ state vector components' covariance envelopes for one week of data processing the full set of observables.

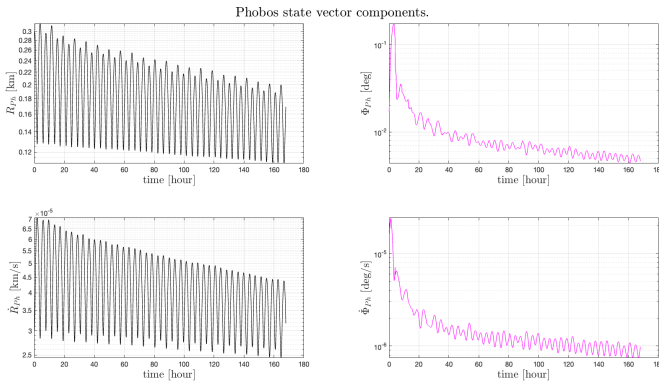


Fig. 9: Phobos's 3σ state vector components' covariance envelopes for one week of data without DSN data.

of a few micro degrees per second. Again, the optical data's contribution to the state vector's uncertainties is evident, as the libration angle's uncertainties are way smaller than what was reported in [7] where optical data were not processed. Clearly, excluding the radiometric data from the estimation chain has a strong impact this time as Phobos's true anomaly cannot be observed anymore and therefore its absolute position in space is not known anymore. As Figure 9 shows though, Mars's limb still allows us to gather some knowledge about the relative position between Phobos and the red planet since, albeit slowly, the radial distance's uncertainties are seen to shrink over time. The moon's libration motion amplitude, which has effects on the spacecraft's dynamics and in the apparent motion of Mars and Deimos in Phobos's sky, can still be observed with high accuracy instead.

B. Phobos gravity field estimation

The spacecraft's capability to observe the moon's gravity field while orbiting orbits with different geometries characterized by the same average altitude was also assessed. The *a priori* covariance for the moon's normalized gravity field's harmonics coefficients, as reported in table III, was assumed to be 1×10^{-2} , and the spacecraft's capability to reduce these uncertainties was assessed by comparing the 3σ covariance envelopes at the end of a three-week long analysis with the

magnitude of the true values of the coefficients. To draw these conclusions, the results obtained processing the full set of observables are compared with the ones for which radiometric data are excluded and the results are reported in Figure 10 and Figure 11.

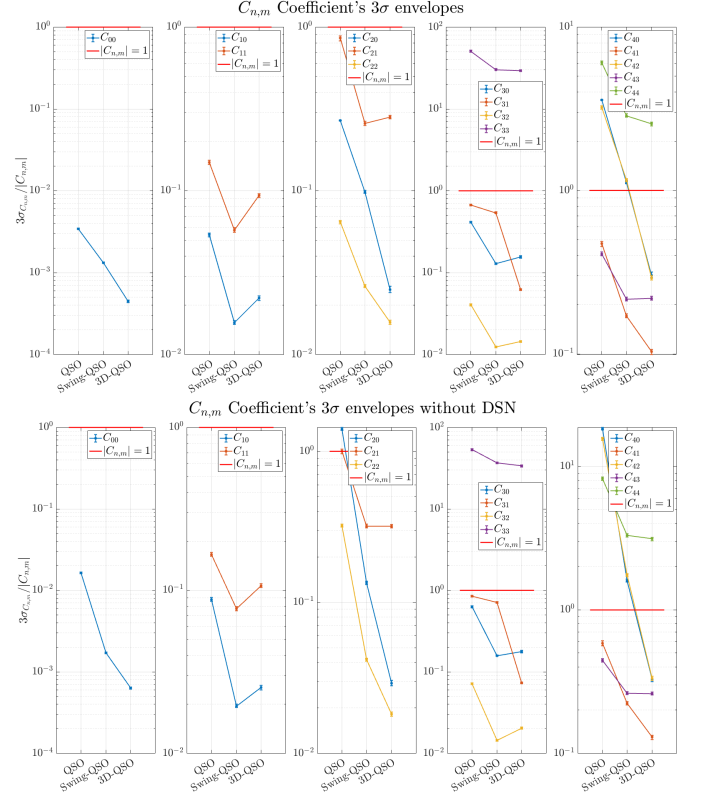


Fig. 10: $C_{n,m}$ coefficients' 3σ covariance envelopes at the end of a two-week long data collection campaign as a fraction of their true value.

Spanning across the results, it can be seen that for many of the gravitational field's harmonics coefficients' uncertainties can be accurately reduced by tracking the Probes' motion in any of the orbit geometries, as the 3σ covariance envelopes decay to a fraction of the true value. However, the uncertainties are seen to decrease further when the spacecraft moves out of the moon's equatorial plane and orbits 3-dimensional trajectories. SwingQSO orbits, despite being still planar, offer an improvement with respect to the QSOs orbits, but the difference is not as marked as the one between the QSOs and the 3DQSOs orbits. Furthermore, the choice between processing or not the radiometric data has a limited impact on the results, as it happened for the spacecraft's state vector components' uncertainties. There is a small improvement in the results when the radiometric data are processed, but the difference is not marked as, with this setup, the observables that have more impact on the whole problem's observability are those directly related to the probe-moon relative position and velocity.

Interestingly the uncertainties on the $C_{2,0}$ and $C_{2,2}$ coefficients, which have direct relations with the moon's moments of inertia, as per [7], can be reduced to almost a 1% of their true

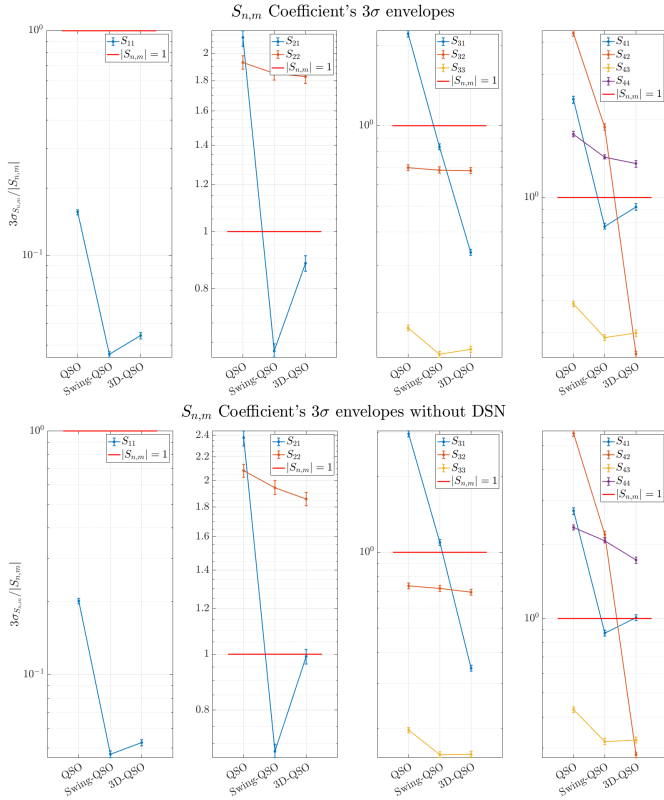


Fig. 11: $S_{n,m}$ coefficients' 3σ covariance envelopes at the end of a two-week long data collection campaign as a fraction of their true value.

value tracking the MMX's motion on the 3DQSO-Lb orbit. Similarly, the fourth degree and order coefficients' uncertainties are seen to be reduced to a 10% of their true value, while, for some of them, planar periodic seem completely unable to observe them. These are important considerations that need to be taken into account being the moon's gravity field and the distribution of its moments of inertia a key factor in the understanding of the moon's internal structure and its formation history.

These results are consistent with the ones reported in [4], [7], where the out-of-plane motion of the spacecraft was seen to be the most effective in reconstructing the moon's gravity field. They also show that the spacecraft's capability to properly observe the moon's gravity field is slightly affected by the elimination of the radiometric data from the estimation chain once the analysis is set up in a relative navigation scenario. Being able to quantify the harmonics gravity coefficients up to this level of detail would be a significant improvement against the results published so far in literature [18]–[20].

VI. CONCLUSION

A covariance analysis was performed to assess the relative navigation performance of MMX around Phobos during the mission's proximity phase, and the spacecraft's capability to observe Phobos's state and gravity field. To do so, the spacecraft's reference trajectories were redesigned in the rotational Mars-Phobos system's dynamics described with

respect to the Phobos's principal body-fixed reference frame, incorporating a fourth-order harmonic expansion of the moon's gravitational potential. These trajectories were then used to simulate the spacecraft's motion and the observables' collection campaigns. The data were finally processed by a UKF-based covariance analysis tool to quantify the state vector components and the moon's spherical harmonics coefficients' uncertainties and their evolution over time.

The analysis focused on highlighting the differences in the spacecraft's navigation performance when the radiometric data were processed or not, comparing the rate of convergence of the state vector components' uncertainties. In this scenario, the observables that are expected to have more impact on the whole problem's observability are those directly related to the probe-moon relative position and velocity. Within this latter group, landmark-based navigation was expected to be fundamental.

As expected, the exclusion of DSN data causes the spacecraft to lose track of the moon's absolute position in space, losing the capability to observe the moon's true anomaly. Nevertheless, the spacecraft is still capable of safely navigating around Phobos, with the optical data being the main source of information. Mars's limb allows us to gather some knowledge about the relative position between Phobos and the red planet, while the moon's libration motion amplitude, which has effects on the spacecraft dynamics and in the apparent motion of Mars and Deimos in Phobos's sky, can still be observed with high accuracy even without the radiometric data. Since the probe's motion is described in the moon's principal body-fixed reference frame, landmarks-based navigation and lidar measurements give enough information to the spacecraft to navigate around the moon with high accuracy. Similarly, the spacecraft's capability to observe the moon's gravity field is slightly worsened by the elimination of the radiometric data from the estimation chain once the analysis is set up in a relative navigation scenario. At the same time, the spacecraft's capability to properly observe the moon's gravity field is seen to be rather affected by the geometry of the orbits, with the 3DQSO orbits being the most effective in reconstructing the moon's gravity field. These results are consistent with the ones reported in [4], [7], underlining the importance of the spacecraft's out-of-plane motion in the observation of the moon's gravity field. These considerations are important for the mission design for the proximity operations as the moon's gravity field and the distribution of its moments of inertia are key factors in the understanding of the moon's internal structure and its formation history [21].

REFERENCES

- [1] K. Matsumoto, N. Hirata, H. Ikeda, T. Kouyama, H. Senshu, K. Yamamoto, H. Noda, H. Miyamoto, A. Araya, H. Araki *et al.*, "Mmx geodesy investigations: science requirements and observation strategy," *Earth, Planets and Space*, vol. 73, pp. 1–15, 2021.
- [2] D. J. Scheeres, "Stability of the planar full 2-body problem," *Celestial Mechanics and Dynamical Astronomy*, vol. 104, pp. 103–128, 2009.
- [3] —, *Orbital motion in strongly perturbed environments: applications to asteroid, comet and planetary satellite orbiters*. Springer, 2016.
- [4] E. Ciccarelli and N. Baresi, "Consider covariance analyses of periodic and quasi-periodic orbits around phobos," in *2021 AAS/AIAA Astrodynamics Specialist Conference*, 2021.

- [5] D. Scheeres, Z. Olikara, N. Baresi *et al.*, “Dynamics in the phobos environment,” *Advances in Space Research*, vol. 63, no. 1, pp. 476–495, 2019.
- [6] N. Baresi and Y. Kawakatsu, “Quasi-periodic motion around phobos: Applications to the martian moons exploration (mmx);” in *32nd International Symposium on Space Technology and Science (ISTS)*. Japan Soc. for Aeronautical and Space Sciences Tokyo, Japan, 2019, pp. 1–8.
- [7] E. Ciccirelli and N. Baresi, “Covariance analysis of periodic and quasi-periodic orbits around phobos with applications to the martian moons exploration mission,” *Astrodynamics*, vol. 7, no. 3, pp. 363–379, 2023.
- [8] B. Schutz, B. Tapley, and G. H. Born, *Statistical orbit determination*. Elsevier, 2004.
- [9] W. Martens and E. Joffre, “Trajectory design for the esa lisa mission,” *The Journal of the Astronautical Sciences*, vol. 68, no. 2, pp. 402–443, 2021.
- [10] C. Bottiglieri, F. Piccolo, A. Rizza, C. Giordano, M. Pugliatti, V. Franzese, F. Ferrari, F. Toppo *et al.*, “Trajectory design and orbit determination of hera’s milani cubesat,” in *2021 AAS/AIAA Astrodynamics Specialist Conference*, 2022, pp. 1–15.
- [11] H. Senshu, T. Mizuno, K. Umetani, T. Nakura, A. Konishi, A. Ogawa, H. Ikeda, K. Matsumoto, H. Noda, Y. Ishihara *et al.*, “Light detection and ranging (lidar) laser altimeter for the martian moons exploration (mmx) spacecraft,” Springer, Tech. Rep., 2021.
- [12] S. Kameda, M. Ozaki, K. Enya, R. Fuse, T. Kouyama, N. Sakatani, H. Suzuki, N. Osada, H. Kato, H. Miyamoto *et al.*, “Design of telescopic nadir imager for geomorphology (tengoo) and observation of surface reflectance by optical chromatic imager (orochi) for the martian moons exploration (mmx),” *Earth, Planets and Space*, vol. 73, pp. 1–14, 2021.
- [13] J. A. Christian, “Optical navigation using planet’s centroid and apparent diameter in image,” *Journal of guidance, control, and dynamics*, vol. 38, no. 2, pp. 192–204, 2015.
- [14] C. X. Wu, P. Machuca, L. Felicetti, and J.-P. Sanchez, “Autonomous optical navigation for small spacecraft in cislunar space,” 2022.
- [15] T. Teil, H. Schaub, and D. Kubitschek, “Centroid and apparent diameter optical navigation on mars orbit,” *Journal of Spacecraft and Rockets*, vol. 58, no. 4, pp. 1107–1119, 2021.
- [16] R. Hu, X. Huang, and C. Xu, “Visual navigation with fast landmark selection based on error analysis for asteroid descent stage,” *Advances in Space Research*, vol. 68, no. 9, pp. 3765–3780, 2021.
- [17] J. Leonard, B. Jones, E. Villalba, and G. Born, “Absolute orbit determination and gravity field recovery for 433 eros using satellite-to-satellite tracking,” in *AIAA/AAS Astrodynamics Specialist Conference*, 2012, p. 4877.
- [18] M. Pätzold, T. Andert, G. Tyler, S. Asmar, B. Häusler, and S. Tellmann, “Phobos mass determination from the very close flyby of mars express in 2010,” *Icarus*, vol. 229, pp. 92–98, 2014.
- [19] R. Jacobson and V. Lainey, “Martian satellite orbits and ephemerides,” *Planetary and space science*, vol. 102, pp. 35–44, 2014.
- [20] X. Yang, J. Yan, T. Andert, M. Ye, M. Pätzold, M. Hahn, W. Jin, F. Li, and J.-P. Barriot, “The second-degree gravity coefficients of phobos from two mars express flybys,” *Monthly Notices of the Royal Astronomical Society*, vol. 490, no. 2, pp. 2007–2012, 2019.
- [21] S. Le Maistre, A. Rivoldini, and P. Rosenblatt, “Signature of phobos’ interior structure in its gravity field and libration,” *Icarus*, vol. 321, pp. 272–290, 2019.